Deep–Sea Research I 167 (2021) 103424

Contents lists available at ScienceDirect

Deep-Sea Research Part I

journal homepage: http://www.elsevier.com/locate/dsri

Hydrodynamics of the choke point between Cape Town and Antarctica during the austral summer of 2019

Alvarinho J. Luis *, Kiledar S. Tomar, Ashutosh Prasad

National Centre for Polar and Ocean Research, Ministry of Earth Sciences, Headland Sada, Goa, 403804, India

ARTICLE INFO

Keywords:
Southern ocean
Hydrological fronts
Water mass
Heat content
Baroclinic transport

ABSTRACT

This study addresses the hydrodynamics inferred from the expendable conductivity-temperature-depth (XCTD) observations carried out in the southwestern Indian Ocean sector of the Southern Ocean along two transects: the Lazarev Sea to Cape Town (track-1) and Cape Town to Prydz bay (track-2) during the austral summer of 2019. The vertical temperature and salinity structures revealed an eddy extending up to 44°S (45°S) on track-1 (track-2). South of the eddy, we encountered frontal zones extending to 53°S (59°S) on track-1(track-2). The frontal locations identified from XCTD and satellite-based sea surface temperature and absolute dynamic topography coincided, with the latter placed within the latitudinal limits identified from the XCTD data. Meandering of the Polar front (PF), the southern Antarctic Circumpolar Current (ACC) Front, and the Southern Boundary of the ACC was observed from 90 to 550 km southward. The Winter Water which was confined to the south of 50°S was detected at deeper depth (~350 m) on track-1, compared to a depth of 100 m on track-2, and its thickness varied from zero to 1.2 m on track-1 and from 0.5 to 2.5 m on track-2. The vertical thermohaline structure revealed the northward subduction of a mixture of Antarctic Surface Water and Subantarctic Surface Water up to 45.5°S and down to 500 (320) m on track-1 (track-2). The volume transport (relative to 1000 m) accounted for 87% of that estimated in the literature (90 ± 2.4 Sv) and 34.7 Sv across track-1 and -2, respectively. It was found that 70% of the volume transport was confined to the ACC frontal region and 26% of the total transport occurred in the 100–500 m slab. The cumulative heat and salt content was 2% and 1.2% higher between 39° and 66°S, compared to that estimated from 2008 data along track-1. We used a satellite-based absolute dynamic topography field, to trace out Agulhas current (AC) and its retroflection current, and eddies detached from the meanders. A higher dynamic topography gradient across the polar front facilitates enhanced transport. Sea surface temperature fields revealed that the meanders in the AC propagate southwest with an offshore extent of 30–300 km.

1. Introduction

The southwest Indian Ocean (IO) sector of the Southern Ocean (SO) is characterized by the Agulhas Current (AC) system in the subtropics, the Antarctic Circumpolar Current (ACC) in the mid-latitudes, and the gyres of the Weddell Sea and Prydz Bay to the south of the ACC domain. The south IO subtropical gyre comprises of the western boundary AC, the Agulhas Return Current (ARC) (Lutjeharms and Ansorge, 2001) which flows east as the South Indian Ocean Current (Stramma, 1992), the West Australian Current, and the South Equatorial Current (Fig. 1). This wind-driven gyral circulation is similar to other gyres in that most of the water recirculates back to the AC from the western and the central south IO (Stramma and Lutjeharms, 1997), resulting in weak feedback circulations west of 70°E (Donohue and Toole, 2003). The AC transports warm and saline water partly into the eastern Atlantic Ocean and partly feeds the ARC.

The IO sector exhibits a complex frontal system with significant regional differences dictated by anomalous features in the bottom topography (Kostianoy et al., 2004). A hydrological front is a zone of enhanced horizontal gradients of water properties that separates the broader areas of different water masses or different vertical structures (Pollard et al., 2002). The ridge systems steer the flow pattern to conserve planetary vorticity (*PV*). In the literature, the choice of a frontal identification has been guided by the objectives of the study and the available data. The frontal positions in the SO have been mapped using the satellite-based surface temperature (T_s), the sea surface height from altimetry (Chambers, 2018; Freeman and Lovenduski, 2016; Kim and Orsi, 2014; Sokolov and Rintoul, 2007; Dong et al., 2006), and the

* Corresponding author.
E-mail addresses: alvluis@ncpor.res.in, alvluis1@gmail.com (A.J. Luis).

https://doi.org/10.1016/j.dsr.2020.103424
Received 8 February 2020; Received in revised form 25 September 2020; Accepted 23 October 2020
Available online 12 November 2020

hydrographic data (Orsi et al., 1995; Belkin and Gordon, 1996 (hereinafter BG96); Swart et al., 2008; Swart and Speich 2010).

The front detection from hydrography often uses a specific criterion of property values at some selected subsurface levels. For example, the most frequently cited level for the PF is the 200-m level, which is traditionally defined as the northernmost extent of the subsurface temperature minimum layer (T_{min}) or the Winter Water (WW) temperature of 2°C (Botnikov, 1963). This definition for the PF has been most widely and probably unanimously accepted in the literature (BG96; Orsi et al., 1995; Park et al., 1993; Whitworth and Nowlin, 1987). The SAF often coincides with the beginning of the northward descent of the salinity minimum layer (S_{min}) (Whitworth and Nowlin, 1987), which can be identified at 400 m coinciding with the 4–5°C isotherms (Orsi et al., 1995) or with the 200-m axial isotherms between 4° and 6°C, depending on the circumpolar locations (BG96). BG96 highlighted the circumpolar robustness of the structural criteria applied to the vertical thermohaline structure/stratification to detect all major SO fronts in the IO sector.

Since the 80s, hydrographic data have been used to delineate fronts (*cf* Orsi et al., 1995; BG96). Since 90s, with the availability of the data from the microwave sensors, T_s (Kostianoy et al., 2004) and the sea surface topography (*cf.* Kostianoy et al., 2004; Sokolov and Rintoul, 2007) have been used to detect the SO fonts. Inferred from the hydrographic data, the AC fronts comprise of the Agulhas Front (AF) and the Agulhas Retroflection (AR) front (ARF). Moving southward, the commonly identified ACC fronts are the north and south Subtropical Fronts (NSTF and SSTF) (BG96), the Subantarctic (SAF), the Polar Front (PF) (BG96), and the southern ACC front (SACCF; Meijers et al., 2010) (Fig. 1). The AF is the eastward extension of the AC, which connects the water from south-western Africa to subtropical and subAntarctic waters (BG96, Kostianoy et al., 2004) The ARF merges with the STF between 40° and 120°E (Fig. 4 in BG96). The southern periphery of the ACC (SB) demarcates the southern limit of the ACC (Orsi et al., 1995).

The ACC fronts delineate the ocean into three zones (Pollard et al., 2002): the Subantarctic Zone (SAZ) extending from the STF to the SAF, the Polar Frontal Zone (PFZ) spanning the SAF to the PF, and the Antarctic Zone (AZ) to the south of the PF (Fig. 1). Due to the presence of numerous jets in the ACC (Sokolov and Rintoul, 2007), the thermohaline properties change rapidly with latitude. Since the ACC exerts a considerable influence on the climate system (Speich et al., 2001), a study on the dynamics of the ACC fronts is necessary.

Three major structural elements have been reported by BG96 for the region to the north of the SAF: (1) The Subantarctic Mode Water which is a >400 m thick, homogenous layer, (2) the intermediate S_{min}, and (3) the subsurface salinity maximum (S_{max}). In contrast to the single jet of the conventional SAF (cf. Orsi et al., 1995), Sokolov and Rintoul (2002) detected three branches of the SAF based on the temperature criteria at 300-400-m depth range, namely, 6–8 °C for the northern branch of the SAF (SAF1), 5–6 °C for the middle branch of the SAF, and 3–5°C for the southern branch of the SAF2. The conventional SAF of Orsi et al. (1995) closely match the middle SAF. Orsi et al. (1995) defined the SACCF at

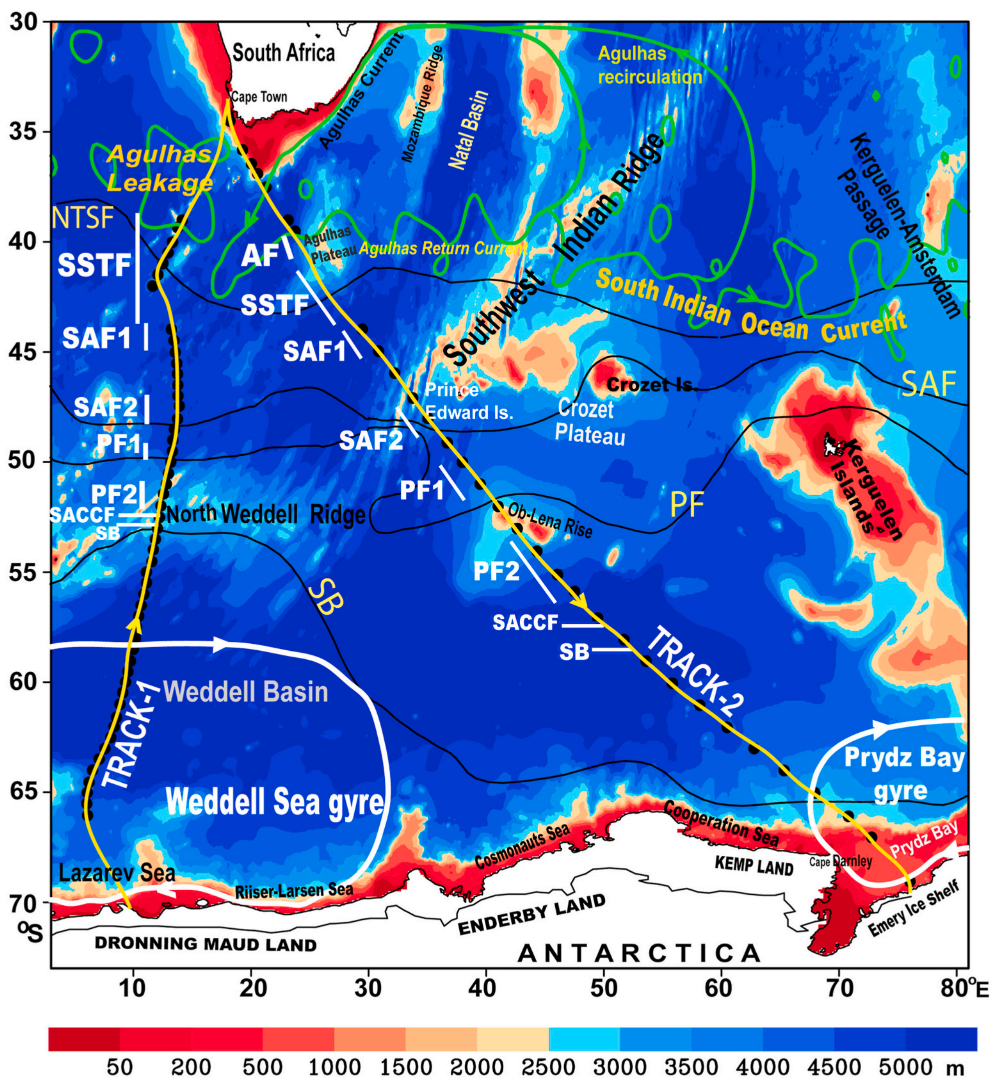

Fig. 1. The geographic features and bathymetry (Smith and Sandwell, 1997) of the study area. ● indicate the locations of the XCTD stations deployed along track-1 and track-2. Following Orsi et al. (1995), the contours of north Subtropical Front (NSTF), Subantarctic Front (SAF), Polar Front (PF), and the Southern boundary of the Antarctic Circumpolar Front (ACC) are shown. The satellite-based dynamic topography (green contour) represented by 0.7 dy m is superimposed to highlight the Agulhas Current, the Agulhas Retroflection, and the Agulhas Return Current. Based on the literature, the schematic of Prydz Bay and the Weddell Sea gyre are also shown. (For interpretation of the references to colour in this figure legend, the reader is referred to the Web version of this article.)

the Greenwich Meridian with $T_{\min}$ close to 0°C at a depth of <150 m or at the subsurface temperature maximum ($T_{\max}$) of 1.8 °C. Likewise, Orsi et al. (1995) used 1.6 °C for $T_{\max}$ to trace the front associated with the SB.

The discrete measurements and the model simulations provide some insights into the overall structure and the variability of the SO fronts but do not resolve the volume transport at the frontal locations. However, the hydrographic snapshot data can provide information on water masses, ACC transport, and the frontal features at the chokepoints such as the Drake Passage, south of Tasman, south of South Africa, where the SO dynamics are constrained meridionally. We have been deploying Expendable CTDs (XCTD) in the southwest IO between South Africa and Antarctica since the fourth International Polar year (2007–2008), by using the ships-of-opportunity, *i.e.*, the cargo ships chartered for the replenishment of provisions and fuel for the Indian Antarctic stations (Maitri and Bharati). The broad objectives of the project are to investigate the role of the upper-ocean hydrodynamics on the sea ice variability and the primary productivity, in the scenario of the SO warming and freshening (Swart et al., 2018).

In this work, we provide insights into the physical oceanographic aspects between Africa and Antarctica focusing on the subtropical domain, the ACC region, and Antarctic sector, using the XCTD data collected aboard the cargo ship M. V. VASILY GOLOVNIN. We focused on two transects: track-1 extended from Cape Town (34.51°S,18.21°E) to Prydz Bay (69.05°S, 76.01°E) which was occupied from 27th January to 6th February, and track-2 was sampled from the Lazarev Sea (66.05°S, 6.11°E) to Cape Town (39.00°S, 14.15°E) from 23rd April to 4th May 2019, respectively (Fig. 1). The goals are (1) to identify the hydrological fronts using XCTD, satellite-based T_s, and altimetry-based dynamic topography, and compare their locations with those inferred in the literature; (2) to relate the hydrographic fronts to water mass boundaries, maxima in zonal transport, and heat/salt content variability.

Fig. 1 depicts the study area, superimposed with the topographic features, contours of major fronts following Orsi et al. (1995), and frontal zones. For comparison, we have overlaid the locations of the fronts identified by the XCTD data along track-1 and -2. The subtropical region shows the schematics of the AC system traced from the dynamic topography data mapped from altimeters (see section 2.2). The schematics to the south indicate the extent of the eastern limb of the Weddell Sea gyre (WSG) and the western limb of the Prydz Bay gyre (PBG). The surface circulation comprises of a closed cyclonic gyre in the vicinity of the Amery Ice Shelf (Smith et al., 1984), which facilitates an influx of cold water from the West Ice Shelf in the east and an offshore flow off Cape Darnley. The WSG is a wind-driven feature, with the circulation veered off by the basin topography, the continental boundaries, and the seabed structures. To the north, the ACC boundary is constraint by the frontal structure, which is in turn topographically steered by the South Scotia Ridge in the west and the North Weddell Ridge in the northeast (Vernet et al., 2019). Along the Antarctic shelf, the easterly winds drive the Antarctic coastal current westward (e.g., Fahrbach et al., 1992).

2. Material and methods

2.1. Hydrographic data

We recorded the profiles of temperature and salinity by deploying XCTDs (manufacturer: Tsurumi-Seiki Co. Ltd, Japan; type: XCTD-3; temperature: ±0.02°C; conductivity: ±0.03 mS/cm; and depth: ±2%; depth range: 1000 m). The XCTD stations (thick dots) deployed along track-1 and track-2 are depicted in Fig. 1. The XCTD probes were deployed at about 30–40 nautical miles interval, except for some locations where their deployment had to be aborted due to the inclement weather. The XCTD profiles were quality controlled by following the guidelines outlined elsewhere (CSIRO Cookbook, 1993; Uchida et al., 2011). Highfrequency noise in the salinity profiles was removed by using a median filter with a 15-m window (Yuan et al., 2004). A comparison of XCTD and Sea Bird CTD profiles revealed that the former was consistent with the manufacturer's specified accuracy for the temperature and salinity (Mizuno and Watanabe, 1998), and the fall rate for XCTD showed no systematic bias in the fall equation given by the manufacturer (Kizu et al., 2008). To facilitate the identification and vertical distribution of water masses, the *T-S* diagrams were prepared (Fig. 2). We have introduced a new way of representing the vertical extent of water masses along the XCTD section in the form of vertical bars (Fig. 3). The criteria adopted for the water masses identification are listed in Table 1.

The special feature of the SO is the formation of the WW during austral summer. It is one of the components of the Antarctic Surface Water (AASW). The WW forms the $T_{\min}$ layer (θ: −1.9° to 1.5 °C and *S*: 34.2 to 34.5 psu) confined to upper 300 m (Park et al., 1998), which is the residual surface water formed by convection (Wong et al., 1998) during the previous winter, and capped by the seasonal warm and freshwater (Deacon 1937). The depth of the WW, its core temperature ($T_{\min}$), and T_s are portrayed in Fig. 4.

The vertical structures of temperature and salinity (Fig. 5b, c, e, f) were prepared by using the XCTD profiles. The hydrological fronts and their locations were detected by using the criteria specified in Table 2. The fronts were identified at their central position, based on the axial property at a particular depth; e.g., the temperature at surface (θ_0) or 200 m (θ_{200}) and surface salinity (S_0) or 200 m (S_{200}) (Park et al., 2001). The front identification and its location were guided by surface expressions (e.g., the spatial gradient in T_s, *S,* and density) (Table 3) and the subsurface features inferred from the vertical structures of the temperature and salinity (Fig. 5).

The baroclinic transport was estimated relative to 1000 m (level of no motion) by using:

$$U_{bc} = \frac{-g}{\rho_0 f} \int_{1000}^{0} \partial_y \rho dz \tag{1}$$

In eq. (1), the surface density (ρ_0) is spatially constant, so we assume that the spatial surface density gradients contribute negligibly to the barotropic transport. The geostrophic transport (Sv) was computed by using:

$$T_g = \int_{y_2}^{y_1} \int_{1000}^{0} U_{bc} dz dy, \tag{2}$$

where *g* is gravity (9.8 m/s^2), the Coriolis parameter f [$= 2 \times 7.29 \times 10^{-5} \times \sin(\text{latitude})$ s^{-1}], y_1 and y_2 are zonal extents. We determined U_{bc} from the density gradients between a consecutive pair of XCTD stations. To account for the variable distance between the hydrographic stations (Fig. 1), we present T_g per 0.5° latitude width in Fig. 6.

The heat (*HC*) and salt content (*SC*) were estimated by integrating the temperature and salinity data from surface to 1000 m (cf. Swart and Speich, 2010):

$$HC = C_p \int_{0}^{1000} \rho \overline{T} dz \tag{3}$$

$$SC = \int_{0}^{1000} 0.001 \rho \overline{S} dz, \tag{4}$$

where ρ is the density of seawater (kgm^{-3}, which was computed using equation of state of Millero and Poisson, 1981), C_p is the heat capacity of seawater at constant pressure (4187 Jkg^{-1}K^{-1}), and $\overline{T}, \overline{S}$ is the average temperature and salinity, respectively, for the layer of thickness *dz* (Fig. 7)

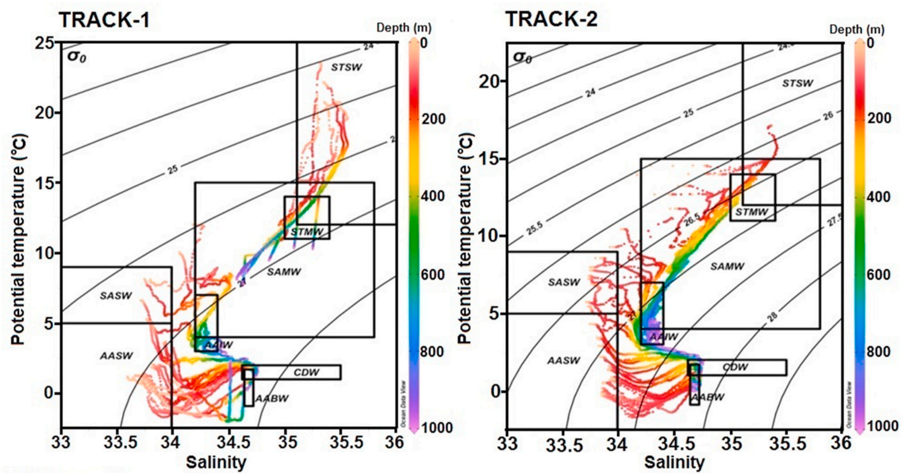

Fig. 2. *T-S* diagram based on the XCTD profiles along track-1 and track-2.

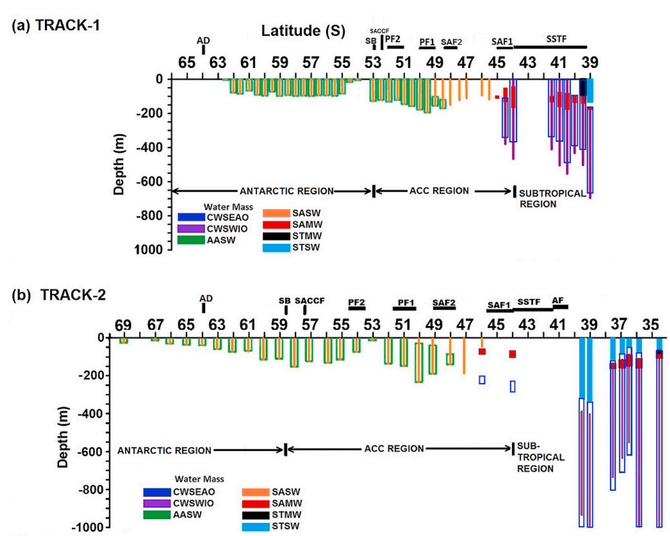

Fig. 3. The vertical extent of water masses identified in the study area. Different ocean regimes are also indicated. The zonal extent of the hydrological fronts is indicated. Abbreviations are CWSEAO - Central Water from Southeast Atlantic Ocean; CWSWIO - Central Water from the southwest Indian Ocean; AASW - Antarctic Surface Water; SASW- Subantarctic Surface Water; SAMW - Subantarctic Mode Water; STMW - Subtropical Mode Water; and STSW - Subtropical Surface Water; SSTF: south Subtropical Front; SAF1 and SAF2: north and south branch of Subantarctic Front, respectively; PF1 and PF2: north and south branch of Polar Front; SACCF: Southern Antarctic Circumpolar Current Front, and SB: Southern Boundary.

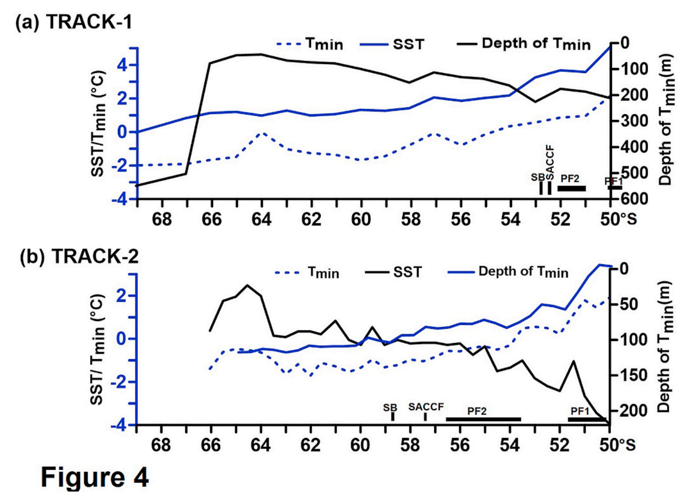

Fig. 4. The zonal extent of Winter Water temperature (T_{min}), depth of T_{min}, and sea surface temperature along track-1 and track-2. The zonal extent of the hydrological fronts is indicated. The fronts are PF1 and PF2: north and south branch of Polar Front; SACCF: Southern Antarctic Circumpolar Current Front, and SB: Southern Boundary.

2.2. Satellite data

The mean absolute dynamic topography (MADT) fields at $1/4^{\circ} \times 1/4^{\circ}$ resolution (product No SEALEVEL_GLO_PHY_L4_NRT_OBSERVATIONS_008_046) were obtained from the European Copernicus Marine Environment Monitoring Service (CMEMS, 2017). These fields were generated by merging all altimeter missions (Jason-3, Sentinel-3A, HY-2A, Saral/AltiKa, Cryosat-2, Jason-2, Jason-1, T/P, ENVISAT, GFO, and ERS1/2) using the optimal interpolation. Since the satellite observations consist of time series of sea surface height, the MADT fields represent the mean stream function of the surface geostrophic flow. These are portrayed in Fig. 8. Based on the 0.7 m MADT contour in Fig. 8, we traced out the AC, its retroflection loop, and the ARC; these have been overlaid on topography shown in Fig. 1 (green contour).

Using the MADT data, we traced out the boundaries of the ACC enveloped by −0.4 m and −1.2 m contours (Dong et al., 2008) in Fig. 8. We used the Tracked Ocean Eddies (TOEddies) automatic detection algorithm (Laxenaire et al., 2018) to confirm the presence of an anticyclonic eddy (also known as Agulhas Rings) at the northern edge of track-1. In brief, the method identifies the local maxima/minima for warm/cold-core in the MADT field as possible eddy centers. Then, it looks for the outermost closed MADT contours around each maximum/minimum containing at least 4 grid points. We also used the T_s fields generated by optimally interpolating the merged microwave and the infrared satellite observations on a $0.09^{\circ} \times 0.09^{\circ}$ resolution (ftp://ftp.remss.com/SST/daily/mw_ir/) to determine the surface gradients at the frontal locations (Fig. 5a, d)

3. Results

In the following sections, we infer the spatial distribution of the water masses (Table 1) with respect to the *T-S* diagram (Fig. 2), and the vertical water-mass extent diagram (Fig. 3). The WW characteristics - T_{min} and its depth are inferred from Fig. 4. The frontal locations and characteristics features are inferred from the vertical structures of

Table 1
Identification criterion of water masses based on hydrological properties.

Water mass	Temp. (°C)	Salinity (psu)	Density (kg m^{-3})	Depth (m)	Reference
Subtropical Surface Water (STSW)	16–28	>35.1		0–200	Valentine et al. (1993)
Subtropical Mode Water (STMW)	11–14	35–35.4	26.5–26.8	400–700	Anilkumar et al. (2015)
Central Water	6–16	34.5–35.5			Valentine et al. (1993)
1.Southeast Atlantic Ocean	8–15	34.6–35.5			Valentine et al. (1993)
2. Southwest Indian Ocean					
Subantarctic Surface Water (SASW)	<9	<34		0–200	Park et al. (1993)
Antarctic Surface Water (AASW)	<5	<34		0–200	Anilkumar et al. (2006) Luis and Sudhakar (2009)
Subantarctic Mode Water (SAMW)	4–15	34.2–35.8	26.5–27.1		
Antarctic Intermediate Water (AAIW)	3–7	34.2–34.4	26.82–27.43	700–1200	Valentine et al. (1993)
Circumpolar Deep Water (CDW)	1–2	34.62–35.5		2000–3800	Anilkumar et al., (2015)

temperature and salinity (Fig. 5). How these fronts influence the volume transport is discussed with reference to Fig. 6, and the highlights of 0–1000 m integrated HC and SC are inferred from Fig. 7. To highlight the dynamics, the regions are demarcated into three zones: the subtropical region extending northward from the southern limit of the SSTF, the ACC region spanning SSTF to SB, and the Antarctic region extending from the south of SB to the Antarctic shelf.

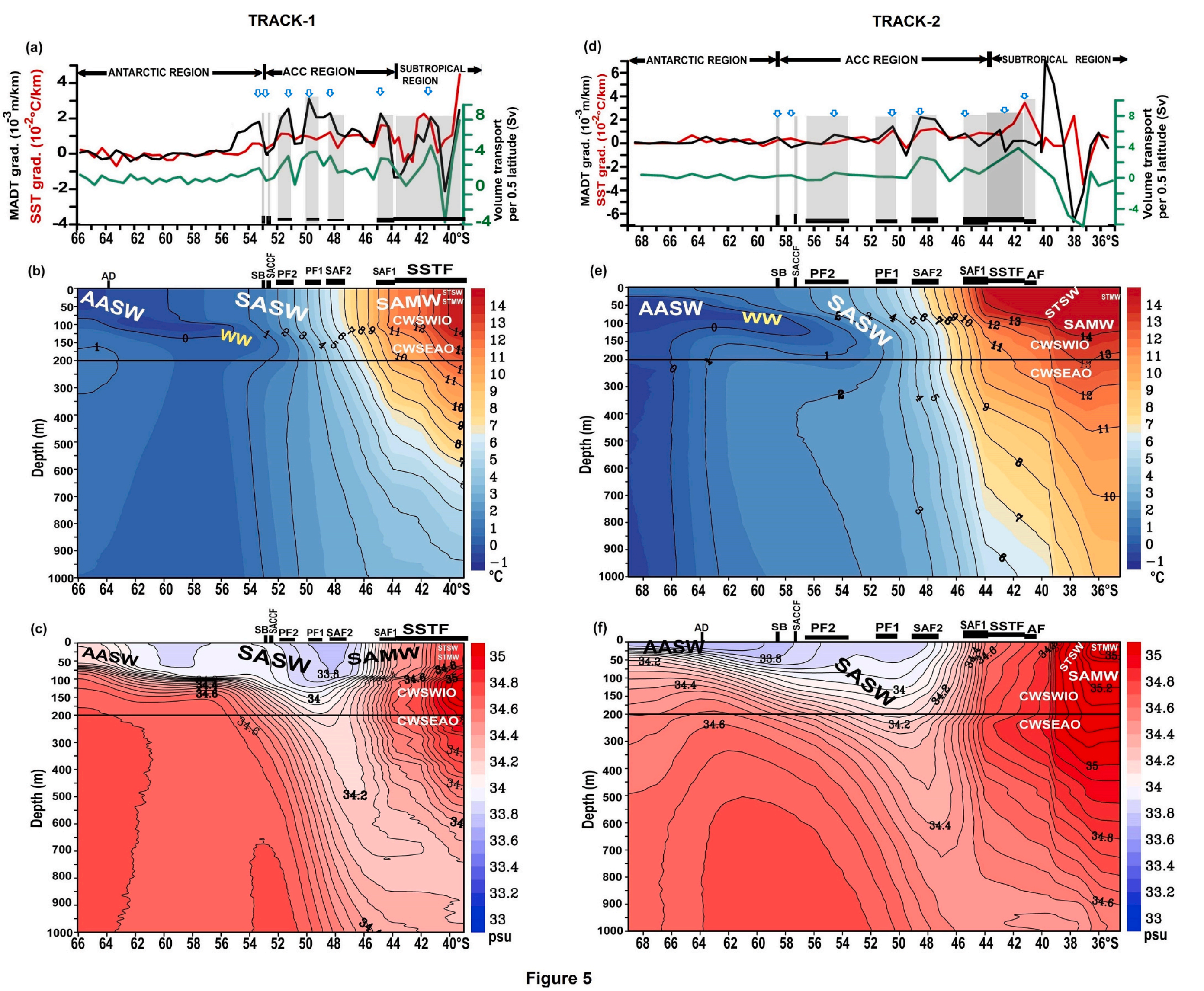

Fig. 5. (a) and (d) Satellite-based MADT and *Ts* gradients, and volume transport per 0.5° latitude width (Sv) for track-1 and track-2, respectively. (b) and (e) The vertical structure of temperature along track-1 and track-2, respectively. (c) and (f) The vertical structure of salinity along track-1 and track-2, respectively. The water masses referred to in this study (Fig. 3) are identified. The different ocean regimes are indicated above the top panel. The vertical arrows in the top panels indicate the central location of the hydrological fronts identified from satellite data. The abbreviations are SSTF: south Subtropical Front; SAF1 and SAF2: north and south branch of Subantarctic front, respectively; PF1 and PF2: north and south branch of Polar front; SACCF: Southern Antarctic Circumpolar Current front, SB: Southern Boundary, and AD: Antarctic divergence.

Table 2
The hydrological properties followed for the identification of hydrological fronts.

Front	Temperature (C)	Salinity (psu)	Reference
Northern Subtropical Front (NSTF)	21–22° at surface	Consistent value of surface salinity of 35.5	Belkin and Gordon (1996); Holliday and Read (1998); Kostianoy et al. (2004)
Agulhas Return Front (AF)	19–17° at surface; 10° isotherm from 300 to 800 m	35.54–35.39 at surface; 35.57–34.90 at 200 m	Holliday and Read (1998); Belkin and Gordon (1996); Sparrow et al. (1996); Kostianoy et al. (2004)
Southern Subtropical Front (SSTF)	17–11° at surface; 12–10° at 100 m	35.35–34.05 at surface; 35–34.6 at 100 m; 34.92–34.42 at 200 m	Holliday and Read (1998); Belkin and Gordon (1996); Sparrow et al. (1996); Kostianoy et al. (2004)
Subantarctic Front (SAF1)	11–9° at surface; 8–5° at 200 m	34.0–33.85 at surface; 34.40–34.11 at 200 m	Holliday and Read (1998); Belkin and Gordon (1996); Sparrow et al. (1996); Park et al. (1993); Kostianoy et al.(2004)
Subantarctic Front (SAF2)	7–6° at surface; 4° isotherm at 200 m	Consistent value of surface salinity of 33.85 south of SAF	Holliday and Read (1998); Peterson and Whitworth (1989); Kostianoy et al. (2004)
Polar Front (PF1)	5–4° at surface northern limit of the 2 isotherm below 200 m	33.8–33.9 at surface	Holliday and Read (1998); Belkin and Gordon (1996); Sparrow et al. (1996); Kostianoy et al. (2004)
Polar Front (PF2)	3–2° at surface	33.8–33.9 at surface	Holliday and Read (1998) Kostianoy et al. (2004)
Southern Antarctic Circumpolar Current Front (SACCF)	Temperature maximum T_{max}> 1.8	Salinity maximum S_{max} > 34:73	Meijers et al. (2010)
Southern Boundary of ACC (SB)	1.5° isotherm		Meijers et al. (2010)

Table 3
Location of the hydrological fronts along the two transects occupied in the southwestern Indian Ocean sector of the Southern Ocean using XCTD and satellite (sea surface temperature and mean absolute dynamic topography derived from altimeters) data.

Front	Front location from XCTD data along		Fronts identified from satellite data		Previously reported locations from hydrographic data, west of 48°E
	Track-1 (°S)	Track-2 (°S)	Track-1 (°S)	Track-2 (°S)	
Agulhas Return Front (AF)	–	40.5–41.3	–	41.3	38°S–41.5°S (Holliday and Read 1998)
Southern Subtropical Front (SSTF)	<43.9	41.3–43.9	41.4	42.7	Observed as a merged front along with ARF and SAF, SSTF is found at about 43°S, 45°E, and between 40°S and 42°S along 55°E, (Holliday and Read 1998)
Subantarctic Front (SAF1)	43.9–45	43.9–45.6	44.8	45.7	44°S–45°S (Kostianoy et al., 2004)
Subantarctic Front (SAF2)	47.4–48.4	47.7–48.9	48.2	48.6	48.5°S–49°S (Kostianoy et al., 2004)
Polar Front (PF1)	49.1–50	50.2–51.7	49.8	50.5	50°S–52°S (Holliday and Read 1998)
Polar Front (PF2)	50.9–52.1	53.6–56.5	51.2	54.6	55°S–57°S (Holliday and Read 1998)
Southern Antarctic Circumpolar Current Front (SACCF)	52.4	57.3	52.8	57.7	c. 60°S–63°S (Meijers et al., 2010)
Southern Boundary of ACC (SB)	52.8	58.7	53.1	58.7	c. 64°S–65°S (Meijers et al., 2010)

3.1. Subtropical region

3.1.1. Water masses

The Subtropical Tropical Surface Water (STSW, θ: 16–28°C, S: >35.1 psu, depth: 0–200 m) in the AC region is comprised of contributions from the southwest IO anticyclonic gyre (Gordon et al., 1987) and water from the Mozambique Channel (Lutjeharms, 1972). The STSW, which is a byproduct of high evaporation in the subtropical zone, is transported by AC to the retroflection region, where it sinks and produces a salinity maximum throughout the south IO (Fig. 2b, c, e, f). We detected the STSW between 39° and 39.5°S along track-1 and from 34.5° to 39.5°S along track-2. The Subtropical Mode Water (STMW) was detected in the upper 100 m at 39.5° and 34.5°S along track-1 and track-2, respectively (Figs. 2 and 3), whereas Tsubouchi et al. (2010) detected its signatures in the domain: 28°–45°S and 60°–80°E.

At the Subtropical Convergence, the mixed subtropical water and the SASW sink to generate the Central Water (CW), which subsequently spreads northward (Orren, 1966). In the AR region, the CW comprises water from South Atlantic Ocean (CWSEA) and southwest IO (CWSWIO). The former is characterized by θ: 8–15 °C and S: 34.6–35.5, while the later is identified by θ: 6–16 °C and S: 34.5–35.5 (Valentine et al., 1993). Since they are synthesized from a blend of thermocline water from the south Atlantic, which entrains into south Agulhas region, and the SASW from the south (Gordon, 1981, 1985), their temperature and salinity ranges are quite close. Both these water masses were detected between 34.5°S and 39.5°S along track-1 and between 39°S

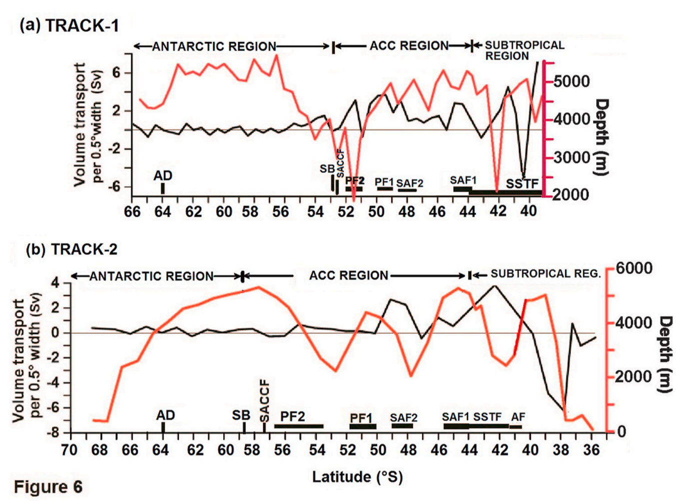

Fig. 6. Volume transport per 0.5° latitude width across track-1 (a) and track-2 (b) estimated from the XCTD data by setting the level-of-no-motion at 1000 m. The different ocean regimes are indicated above each panel. The zonal extent of the hydrological fronts is also indicated.

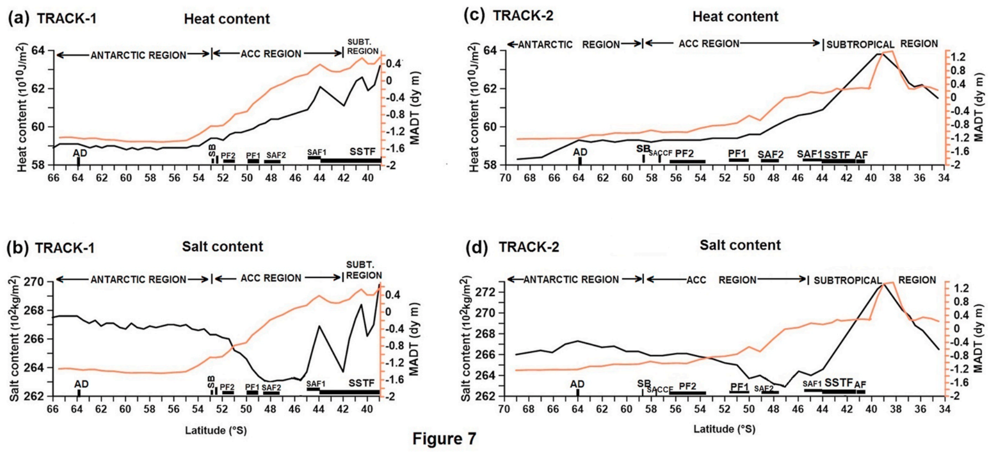

Fig. 7. Heat and salt content integrated from the surface to 1000 m estimated from the XCTD data along track-1 and track-2. The different ocean regimes are indicated above each panel. The zonal extent of the hydrological fronts (identified in Fig. 5) is also indicated. A satellite-based MADT profile is superimposed to gain insight into the linkage between different regimes influenced by circulation.

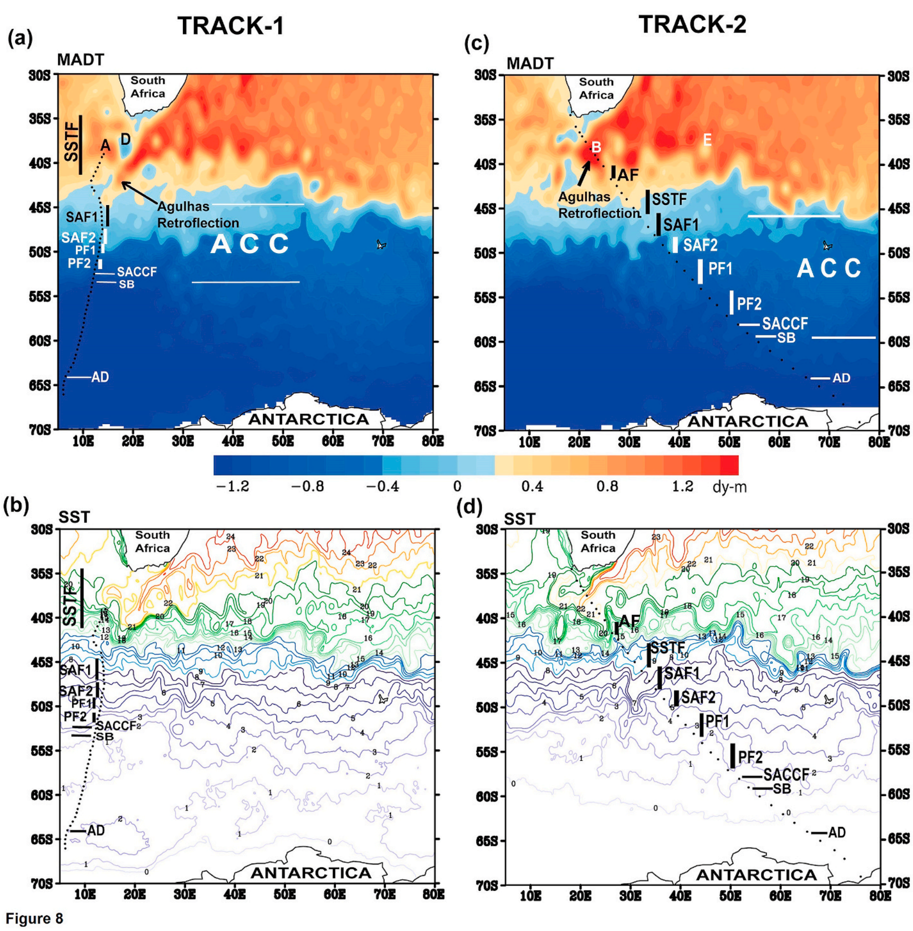

Fig. 8. The merged altimetry-based mean absolute dynamic topography and blended microwave and the infrared observations of sea surface temperature fields were averaged for the sampling period for track-1 (left-hand side panel) and track-2 (right-hand side panel). The zonal extent of the hydrological fronts is indicated. The MADT contours −0.4 and −1.2 delineates the north and south boundary of the ACC, respectively (Dong et al., 2008). The abbreviations are SSTF: south Subtropical Front; SAF1 and SAF2: north and south branch of Subantarctic front, respectively; PF1 and PF2: north and south branch of Polar front; SACCF: Southern Antarctic Circumpolar Current Front, SB: Southern Boundary, and AD: Antarctic divergence.

and 44.5°S along track-2. They were encountered in the upper120 m to the north of 39.5°S and below 200 m to the south of 40°S.

3.1.2. Thermohaline structure and hydrological fronts

The northern edge of track-1 is characterized by the Agulhas anticyclonic eddy (AAE) with its core placed at 39°S. It was characterized by $\theta = 14$°C and $S = 34.8$, and the gradient of MADT/SST of 4×10^{-3} m/km/3×10^{-2} °C/km. The AF, NSTF, and ARF were not traceable, as the data collection had to be terminated at 39°S due to inclement weather. At the southern terminus of the eddy, the SSTF was detected at 42.1°S, which was characterized by the MADT/SST gradient of 1×10^{-3} m/km/2×10^{-2} °C/km. The SSTF serves as a virtual boundary between cooler fresher Subantarctic Surface Water (SASW) from the Subtropical Surface Water (STSW) and delineates the northern periphery of the ACC (Deacon, 1937).

Along the track-2, the AF was encountered between 40.5° and 41.28°S. Following the criteria of Orsi et al. (1995), we traced the location of the SSTF extending from 41.3° to 43.9°S. It is noted that a southward shift in the location of the SSTF from a mean position of 42.9°S (Orsi et al., 1995) to 42.2°S is due to the need to conserve $PV = (f + \zeta)/H$, where $f = 2 \times 7.29 \times 10^{-5} \times \sin(\Theta)$ is planetary vorticity (s^{-1}), ξ is relative vorticity (s^{-1}), Θ is latitude (radians), and H is the water depth (m). In open ocean areas, f is much larger than ζ, so the mean potential vorticity can be approximated by f/H. A large gradient in the bathymetry with 5400 m in the Agulhas Basin to 3200 m over the southern portion of the Southwest Indian Ridge increases f/H eastward ($1.8 \times 10^{-8} s^{-1}$), so the jets associated with SSTF steer northward to conserve the *PV*.

3.1.3. Volume transport

The net volume transport in the upper 1000 m across track-1 amounted to 48 Sv, of which 12.3 Sv was confined to the subtropical domain. The net transport associated with SSTF was 12.3 Sv, of which 10.6 Sv occurred in the upper 500 m. On the other hand, the net transport across track-2 was estimated as 34.7 Sv, of which 2.2Sv were confined to the subtropical regime. A large difference in the net volume since the track-2 is nearly 45° inclined compared to the near-meridional track-1, and since the stations are sparsely placed there is an underestimate in the geostrophic velocity between the pair of stations. It is observed that when the depth of the water column increased the transport was substantially reduced vis-à-vis the shallow regions.

3.1.4. Heat and salt content

The total HC and SC for the stations along track-1 in the subtropical domain amounted to 620×10^{10} J/m^2 and 2665×10^2 kg/m^2. A high peak at 39°S with a corresponding value of 63×10^{10} J/m^2 and 270×10^2 kg/m^2 in the HC and SC, was due to the presence of AAE. Its presence and location is also detected in the MADT field indicated by the letter “A” in Fig. 8. A secondary peak with HC and SC values of 62.6×10^{10} J/m^2 and 268×10^2 kg/m^2, respectively, was encountered at 40.5°S, which coincided with the SSTF. A tertiary peak was encountered at 43.9°S corresponding to sharp gradients in temperature and salinity observed in Fig. 5b and c. The scenario at track-2 is different, where high peaks in HC (63.8×10^{10} J/m^2) and SC (272×10^2 kg/m^2) were detected between 39° and 39.5°S, which coincided with the AC. The total HC and SC in the subtropical region along track-1 amounted to 499 $\times 10^{10}$ J/m^2 and 2153×10^2 kg/m^2, which were ~24% lower compared to those values obtained for track-1. The MADT profile along the ship track is depicted along with the HC and SC profile which confirms the changes observed from the hydrographic data.

In summary, along track-1, the SSTF and AF were dominated by CWSEAO and CWSWIO in the upper 650 m with a trace of STSW at 39° and STMW at 39.5°S in the upper 100 m, while on track-2, CWSEO and CWSWIO occupied almost the entire water column, STSW was found in the upper 300 m, and a trace of STMW was detected at 34.8°S. Sharp gradients in Ts and MADT coincided with SSTF (and AF on track-2) which were detected using the hydrographic data. The maximum volume transport associated with SSTF was 15 (36 Sv) on track-1(track-2) and it exhibited enhanced HC/SC due to the southward transport of the warm/salty tropical waters by AC.

3.2. ACC region

The ACC fronts span over a large extent from the south of the SSTF to the SB, which includes the SAF1 and SAF2, PF1 and PF2, the SACCF, and the SB. Similar to the subtropical region, we highlight the characteristic features in water mass, fronts, volume transport, and heat/salt content.

3.2.1. Water masses

A trace of the STMW was detected between 44 and 44.5°S, from the surface to 330 m on track-1, while on track-2 it was encountered between 44° and 46°S, in the depth range 200–280 m. The SAMW was detected from 44° to 45°S, in the depth range 50–200 m on track-1, while on track-2 it was encountered between 44° and 46°S from 60 to 100 m. The northern extent of the AASW was found to be 48.5° and 48°S on track-1 and track-2, respectively. Its vertical extent on track-1 varied from 100 to 180 m at SAF2 and from the surface to 130 m at the SB, while on track-2, we encountered it at a maximum depth of 218 m at 50°S and 110 m at the SB. The SASW was detected southward of 45.5°S on both tracks. Its vertical extent spanned from surface to ~130 m at the SAF1 and the SB on track-1, while on track-2, it was detected down to 240 m in the SAF2 band.

The WW, which is one of the components of AASW, forms a minimum temperature layer extending southward from the Antarctic shelf to the PF1. In the ACC domain, we found traces of WW to the south of SAF2 between 100 and 220 m on both tracks. On track-1, the temperature of WW (T_{min}) and its depth was 0.8°C and 200 m on average, respectively. On track-2 (track-1), the WW was detected at a shallow depth of 100 (130) m to the south of PF2.

3.2.2. Thermohaline structure and hydrological fronts

The transition between the SSTF to SAF1 is marked by a decrease in T_s from 14° to 10°C and a surface salinity drop from 34.8 to 34. The vertical structure of temperature and salinity showed sharp gradients in the isolines in the SAF1 domain, where the northern limit of the SASW ends (Fig. 3). The advection of the AASW creates a tongue of low salinity (34–34.2) which descends to ~500 m in the midway of the section. The ACC which occupies 1200 km at 10°E meanders southward with its extent widening to ~2200 km at 70°E. The SAF1 was located in the latitudinal band of 43.93°–45°S, within ±2° of the SAF reported by Lutjeharms and Valentine (1984), while on track-2 it spanned from 43.9° to 45.56°S. The SAF2 was encountered between 47.45° and 48.4°S which was marked by the MADT/SST gradient of 0.5×10^{-3} m/km/0.5 $\times 10^{-2}$ °C/km. However, it was traced between 47.74°S and 48.9°S on track-2. We note that the PF1 meandered southward from 49.15° to 50°S to 50.2°-51.74°S on track-2, likewise, PF2 showed a southward shift from 50.9° to 52.1°S to 53.63°-56.52°S on track-2. The largest shift in the location of SACCF was detected from 52.4°S on track-1 to 57.3°S on track-2; likewise, SB meandered about 5° southward from 52.86°S on track-1 to 58.73°S on track-2.

3.2.3. Volume transport

The volume transport across track-2 was found to be 31.4 Sv, with 6.9 Sv confined to 0–100m, 19 Sv was associated with 100–500 m slab and 5 Sv was confined to 500–1000 m slab. Higher transport occurred in the 0–100 m slab and the transport associated with SAF1, SAF2, PF1, and PF2 was found to be 5.9, 4.3, 7.4, and 4.3 Sv, respectively. The net volume transport across track-2 was estimated to be 27.4 Sv, of which 1.7 Sv was confined to the 0–100 m slab, 4.8 Sv to the 100–500 m, and 4.9 Sv to the 500–1000 m slab. Most of the transport associated with the SAF1 (24 Sv), SAF2 (20 Sv), PF1 (11 Sv), and PF2 (0.4 Sv) was confined to the upper 100 m. The uniform density between SACCF and SB facilitated weak transport of 1 Sv across track-1 and 0.3 Sv across track-1.

3.2.4. Heat and salt content

The HC/SC for the ACC domain was found to be 1668×10^{10} J/m^2/ 7431×10^2 kg/m^2 for track-1. The HC/SC decreased by 2×10^{10} J/m^2/ 4×10^2 kg/m^2 from the SAF1 to the SB, due to the northward advection of cold and fresh AASW and SASW in the upper 200 m (Fig. 3a). On the other hand, along track-2, the HC and SC decreased by ~45% from the SAF1 to the SB. This is attributed to the subduction of WW to the deeper depths compared to that at track-1 (Fig. 4), and also due to the extension of the tongue of the SASW toward the SAF2 location. The total HC and SC for the ACC domain were found to be 895×10^{10} J/m^2 and 3974×10^2 kg/m^2, respectively.

In brief, we detected the CWSEAO and CWSWIO in the upper 450 m, the SAMW in the upper 200 m at the SAF1 which was marked by a volume transport of 5.9 Sv and HC/SC of 61×10^{10} J/m^2/264×10^2 kg/m^2 on track-1. On track-2, we found traces of CWSEAO (at ~250 m) and SAMW (at ~75 m) at the SAF1 which was marked by a high volume transport of 24 Sv and HC/SC of 61 × 10^{10} J/m^2/265 × 10^2 kg/m^2. With the presence of SASW in the upper 150 m, the SAF2 on track-1 was marked by a volume transport of 4.3 Sv and HC/SC of 60 × 10^{10} J/m^2/263 × 10^2 kg/m^2, while on track-2, we detected SASW and AASW in the upper 250 m at SAF2 which was marked by volume transport 20 Sv, and HC/SC of 60 × 10^{10} J/m^2/263 × 10^2 kg/m^2. The PF1 meandered southward by ~100 km on track-2 since it encountered a deeper ocean and consequently the volume transport showed an increase from 7 Sv on track-1 to 11 Sv. The bathymetric gradient veered the PF2 southward by ~160 km, but the volume transport is reduced by 90% due to northward spreading of WW and its mixing with ambient water which renders nearly constant HC/SC for both tracks. The WW which was confined to the south of 50°S was detected at deeper depth (~350 m) on track-1, compared to a depth of 100 m on track-2 and its thickness varied from zero to 1.2 m on track-1 and from 0.5 to 2.5 m on track-2.

3.3. *Antarctic region*

Since the water properties do not change drastically, we summarize the results pertaining to the water masses, fronts and vertical structure, volume transport, and heat/salt flux for the domain south of the SB. In this region we detected AASW and SASW, with a vertical extent from the surface to ~100 m, on both tracks; these water masses spread northward due to the upwelling at AD (Fig. 5b, c, e, f). The WW was detected in the upper 100 m from SB to 66°S which was characterized by T_{min} of −1.1°C (on average) on track-1 (Fig. 4a), while on track-2, its depth varied from 122 m near SB to near-surface at the Antarctic Divergence (AD), with its temperature near to −1.4°C (Fig. 4b). No traces of AAIW (θ: 2.2 °C and a salinity minimum of ~33.87) or AABW were detected, possibly because 1000 m was the terminal depth of the profiles.

In the Prydz Bay, the isolines showed a gradual descend off the shelf and were characterized by a low temperature (1°C) and low salinity (33.8) at the surface due to the glacial runoffs. A layer of freshwater was detected in the upper 30 m which capped the high salinity water below 50 m. It occupied the entire column south of AD on both tracks. Middleton and Humphries (1989) analysis of wintertime observations showed that the saltiest water (34.6) dominated the Prydz Bay shelf. Our section provides evidence for the presence of shelf water along the continental slope, which was missed out by Middleton and Humphries (1989).

The volume transport across track-1 for the 0–1000 m slab amounted to 4.4 Sv, with 1.2 Sv confined to the 105–500 m slab, and 2.4 Sv confined to the 550–1000 m slab. On the other hand, across track-2 a transport of 5.1 Sv was associated with the 0–1000 m slab, with 0.4 Sv confined to the 0–100 m slab, 1 Sv associated with the 105–500 m layer, and 0.9 Sv occurred in the 550–1000 m slab. The total HC/SC was estimated to be 826 × 10^{10} J/m^2/3741 × 10^2 kg/m^2 along track-1. However, along track-2, the HC/SC decreased by 35%/36% from the respective values estimated for track-1.

The Scotia Front (SF) which envelops the Weddell–Scotia Confluence in the north was placed at 54°S, based on the extent of the 1°C isotherm from 300 to 500 m (BG96). It was characterized by weak gradients of MADT (0.8 × 10^{-3} m/km)/SST (0.35 × 10^{-2}°C/km) (Fig. 5a and b). AD, which is a zone of an intense upwelling of CDW (Park et al., 1998), was encountered at 53.8°S, coinciding with a thin WW layer. Using the XCTD observations recorded in the austral summer of 2007, its location was placed at 53.4°S (Luis and Pednekar, 2010). The Antarctic Ice boundary (Park et al., 1998; BG96; Klyausov, 1983) was encountered at 50°S, which was identified based on surface salinity minimum (~33.8), and a 1°C change in *Ts* across the boundary.

In summary, the Antarctic region, which extended to the shelf from 53°S (58.8°) on track-1 (track-2), was dominated by the AASW and SASW from surface to ~100 m (180). These water masses spread northward from the upwelling belt at AD. On track-1 (track-2), the WW was marked by a minimum temperature of −1.1°C (−1.4°) and occupied upper 100 m (122) from SB to 66°S (AD). Our data captured a layer of freshwater (θ = 1°C, S = 33.8) in the upper 30 m capped the high salinity water below 50 m, which descended the continental slope and occupied the entire water column, to the south of AD. The volume transport across track-1 (track-2) amounted to 4.4 Sv (5.1), while the HC/SC was found to be reduced by 35%/36% compared to that for track-1, due to the sinking of the cold and low saline AASW and SASW.

4. Satellite observations

One of the conspicuous features captured in the MADT field was the meandering of AR and detachment of several cold-core eddies marked by low MADT (0.4–0.8 m) in the central south IO (see "C" in Fig. 8c). These satellite-based fields also showed eddies veering off into the eastern Atlantic Ocean from the AR characterized by a warm core with higher MADT (1.2 m, letter "A" in Fig. 8a) and cold-core eddies with lower MADT (−0.1 m, "D" in Fig. 8a and "C" in Fig. 8c). It was observed that the 1.4-m contour of MADT and the 22–24°C isotherms roughly circumscribed the rim of the AC, while MADT/*Ts* of 0.9 m/18°C enveloped the AR and ARC (Fig. 8a–d).

The ACC fronts and the associated water masses distribution usually generate different gradients in sea surface height in the SO. In terms of the MADT/*Ts* gradients, the hydrological fronts exhibit the following characteristics. Along track-1, the SSTF showed the MADT/*Ts* gradient of 0.15 × 10^{-3}m/km/0.71 × 10^{-2}°C/km. In the ACC region, the SAF1 was characterized by the MADT/*Ts* gradient of 1.30 × 10^{-3}m/km/1 × 10^{-2}°C/km, the SAF2 with the MADT/*Ts* gradient of 1.0 × 10^{-3}°m/km/0.7 × 10^{-2}°C/km, the PF1 with a gradient of 1.7 × 10^{-3}m/km/0.6 × 10^{-2}°C/km, and the PF2 occupied the region with MADT/*Ts* gradient of 1.5 × 10^{-3}°m/km/0.8°C/km. Weak gradients across SSTF was due to the transport of warm water by the AC toward the Agulhas Plateau, which increased the heat and salt content (Fig. 7). An elevated MADT gradient across PF1 facilitated enhanced transport (Fig. 6) due to spatial decoupling between cores of the current (Fig. 5), resulting in lower heat and salt content (Fig. 7).

Along track-2, the AF was characterized by a MADT/*Ts* gradient of −0.003 × 10^{-3}m/km/1.6 × 10^{-2}°C/km, and SSTF with a MADT/*Ts* gradient of 0.26 × 10^{-3}m/km/0.79 × 10^{-2}°C/km. In the ACC domain, the SAF1 was marked by a MADT/*Ts* gradient of 0.18 × 10^{-3}m/km/0.44 × 10^{-2}°C/km, the SAF2 with a MADT/*Ts* gradient of 1.5 × 10^{-3}m/km/0.62 × 10^{-2}°C/km, the PF1 with a MADT/*Ts* gradient of 0.6 × 10^{-3}m/km/0.36 × 10^{-2}°C/km, and PF2 with a MADT/*Ts* gradient of 0.24 × 10^{-3}m/km/0.1 × 10^{-2}°C/km. The weak MADT gradient across AF was attributed to strong mixing in the retroflection region over the Agulhas plateau. On the other hand, the highest MADT gradient across SAF2 coincided with enhanced volume transport (Fig. 6) and a drop in the heat and salt content (Fig. 7). In brief, satellite-based MADT and *Ts* maps provided a linkage of surface features to the hydrodynamics inferred from the in-situ observations.

5. Discussion

The frontal locations from this work were compared with those from literature (Table 2). Overall, the frontal position identified from XCTD and satellite-based surface parameters agree well, with the latter placed within the latitudinal extent inferred from the XCTD data. The only exception was with SACCF and SB, which were traced southward in satellite data, possibly because the XCTD stations were far apart. The SSTF is the broadest frontal zone comprising of several fronts delineated by zones of relatively homogenous waters (Lutjeharms et al., 1993). Based on the surface temperature characteristics, the mean position of the STF, between 20°W and 60°E, was reported to be 42°S (Lutjeharms and Valentine, 1984), based on the historical hydrographic data BG96 placed it at 43°S, while Park et al. (2001) identified the SSTF at 42°S by using the CIVA2 data. Anilkumar et al. (2006) detected SSTF coalesced with the northern Subantarctic Front (SAF1) and the ARF to form a merged front called the Crozet Triple Front (BG96) between 40.3° and

43°S, along 45°E.

The SAF is the northern front of the ACC, where a rapid descent of the subsurface salinity minimum of 33.8 psu (BG96; Holliday and Reed, 1998) occurs. Its location is at the point from where the northward spread of Antarctic Intermediate Water (AAIW) below 400 m takes place. The SAF was found to occupy a width of 1.5° latitude along 45°E (Holliday and Reed, 1998). It has been widely reported that the SAF splits into two branches: the northern SAF (SAF1) and the southern SAF (SAF2) (BG96; Luis and Sudhakar, 2009; Sokolov and Rintoul, 2007; Anilkumar et al., 2015). The SAF1 was located in the latitudinal band of 43.93°–45°S, within the 2° width of the SAF, as reported by Lutjeharms and Valentine (1984). The SAF2 which was encountered between 47.45° and 48.4°S in this work, was placed between 44°S and 44.7°S using XCTD data collected in the austral summer of 2007 along a transect that coincided with track-1 (Luis and Pednekar, 2010).

The large undulations in the bottom topography in the SO force the hydrological fronts to meander to conserve the *PV (=f/D)*. When the ACC jets flow over the mid-oceanic ridges, there is a significant change in the depth, so they are unable to move along the circumpolar trajectories of constant *PV* (Koblinsky, 1990). For example, the AC encounters a steep gradient in the bathymetry between Agulhas Bank (500 m) and ~5° south of Cape Town (where the depth is 5000 m) (Fig. 1), so *PV* is conserved by increasing *f, i.e.,* by veering off its path toward the south Atlantic Ocean. In this situation, the AR occurred at about 18°E, 43°S on track-1, and at 23°E, 40°S on track-2 (Fig. 8a, d). Likewise, the PF1 on track-1 was placed at a mean location of 49.5°E, below which the depth is 4700 m, meandered southward to 50.9°S on track-2, where the depth increased to 4480 m (Fig. 6). Similarly, PF2 which was traced at 51.5°S on track-1, where the depth was ~2000 m, meandered southward to the deeper ocean (4000 m) where its mean location was 55.2°S on track-2.

It is also inferred in the literature that the positive SAM shifts the westerly wind zone southward, resulting in southward displacement in the ACC circulation. Graham et al. (2012) elucidated the role of winds and the bottom topography on the meandering process of the SO fronts, based on the control/climate change simulation using a high-resolution coupled climate model. They inferred that: (1) the bottom topography influences the intensity of fronts, not on the position/spacing of the frontal jets, (2) the increasing speed of the westerlies are effective in shifting fronts southward by 1.3°, with no significant displacement of the ACC path or its fronts meridionally, and (3) the STF is displaced towards south gradually over steep topography, implying that the STF is strongly surface intensified.

The vertical temperature and salinity structures captured an anticyclone centered at 39°S, 15°E on track-1. The satellite-based MADT/*Ts* fields revealed that the retroflection occurs between 40° and 43°S on both the tracks. To the south of this latitude, we encountered strong frontal zones extending to 52.86°S (58.73°S) on track-1(track-2). A tongue of WW was detected from near-surface at the Antarctica shelf down to 550 (220 m) at 69°S (50°S) on track-1 (track-2). The WW was detected from the surface to 1.2 m on track-1 and between 0.5 and 2.5 m on track-2. The important feature identified was the northward subduction of a mixture of the AASW and the SASW water down to 500 m on track-1, which was traced to 320 m on track-2 (Figs. 3–5). Its northern extent was close to 50°S on both the tracks (Fig. 5).

The volume transport estimated along track-1 amounted to 87% of that estimated in the literature (90 ± 2.4 Sv), which the calculation was restricted to 1000 m and the track location was different from that surveyed by other researchers (Table 4). It was found that 70% of the volume transport was restricted to ACC fronts and 26% of the total transport occurred in the 100–500m slab, in agreement with our earlier work (Luis and Pednekar, 2010). It is noted that the cumulative HC and SC was 2% and 1.2% higher for stations between 39° and 66°S, compared to that for 2008 data collected on a similar track coinciding with track-1. This suggests that the upper-ocean (0–1000 m) has warmed possibly due to enhanced transport of warm and saline water from the tropical/subtropical region over the period.

Temperature data obtained from Autonomous Lagrangian Circulation Explorer floats (700–1100 m) in the SO indicated a 0.17°C warming in the mid-depth of the ACC domain during the 1950s and the 1980s, which is comparable to the rate of change in the air temperature in the SO (Gille, 2002). For a decade, the positive phase of the SAM has enhanced the westerly winds over the Antarctic Zone and Polar Frontal Zone, resulting in enhanced equatorward Ekman transport and cold *Ts* anomalies towards these regions (Lovenduski and Gruber, 2005). Since this study lacks a detailed comparison with the previous year's data, concerted efforts will be made to compare the results of previous years to discern interannual variability in the southwest IO sector.

6. Conclusions

The XCTD data and satellite-based *Ts* and MADT were used to trace out the locations of the hydrological fronts along two-ship transects occupied between the choke point between Africa and Antarctica during the austral summer of 2019. We divided the regions into three sectors: the subtropical domain, the ACC region, and the Antarctic domain based on hydrodynamics. The data along two tracks were also compared and the findings of our work can be summarized as follows. The vertical temperature and salinity structures revealed an eddy extending up to 44°S (45°S) on track-1 (track-2). South of the eddy, we encountered frontal zones extending to 53°S (59°S) on track-1 (track-2). At the locations of the SSTF and AF, we detected CWSEAO and CWSWIO in the upper 650 m, with a trace of STSW and STMW in the upper 100 m on track-1, while the CWSEAO and CWSWIO occupied almost the entire water column, with STSW detected in the upper 300 m, and a trace of STMW found at 34.8°S on track-2. Sharp gradients in satellite-based *Ts* and MADT coincided with SSTF (and AF on track-2). The maximum volume transport associated with SSTF was 15 (36 Sv) on track-1(track-2) and it exhibited enhanced HC/SC due to the southward transport of the warm/salty tropical waters by AC.

In the ACC domain, along track-1 we detected the CWSEAO and CWSWIO in the upper 450 m, with the presence of SAMW in the upper 200 m at the SAF1 which was marked by a volume transport of 5.9 Sv and HC/SC of 61 × 10^{10} J/m^2/264 × 10^2 kg/m^2. On track-2, we found traces of CWSEAO (at ~250 m) and SAMW (at ~75 m) at the SAF1 which was characterized by a volume transport of 24 Sv, and HC/SC of 61 × 10^{10} J/m^2/265 × 10^2 kg/m^2. With the SASW found in the upper 150 m on track-1, the SAF2 was marked by a volume transport of 4.3 Sv and HC/SC of 60 × 10^{10} J/m^2/263 × 10^2 kg/m^2. The SAF2 at track-2

Table 4
Comparison of baroclinic transport estimates from our data and those from literature in the study area.

Reference	Transport estimate (Sv)	Hydrographic section
Georgi and Toole (1982)	137	SR1
Whitworth (1985)	134 ± 11.2	SR1
Macdonald and Wunsch (1996)	142 ± 5	SR1, static inverse model
Ganachaud and Wunsch (2000)	140 ± 6	SR1, static inverse model
Ganachaud and Wunsch (2000)	157 ± 10	SR3, static inverse model
Sloyan and Rintoul (2001)	135 ± 1	SR1, static inverse model
Rintoul and Sokolov (2001)	147 ± 10	SR3
Cunningham et al. (2003)	136.7 ± 7.8	ISOS, SR1, deepest common level
Mazloff et al. (2010)	153 ± 5	SR1, assimilating model
Mazloff et al. (2010)	154 ± 5	SR2, assimilating model
Mazloff et al. (2010)	164 ± 6	SR3, assimilating model
Renault et al. (2011)	145 ± 8.8, 137.9 ± 10.5	SR1, direct velocity measurements
Present study (2019)	129 (between 41.24 and 3.74°S)	XCTD data (0–1000 m)

was characterized by the presence of SASW and AASW in the upper 250 m, a volume transport of 20 Sv, and an HC/SC of 60×10^{10} J/m^2/263 $\times 10^2$ kg/m^2. The PF1 meandered southward by ~100 km on track-2 since it encountered a deeper ocean and consequently the volume transport showed an increase from 7 Sv (on track-1) to 11 Sv. The PF2 also shifted southward by ~160 km with an increase in depth of 2000 m, but the volume transport is reduced by 90% due to northward spreading of WW and its mixing with ambient water which rendered nearly the same HC/SC at 59×10^{10} J/m^2/265 $\times 10^2$ kg/m^2 on both tracks. The WW which was confined to the south of 50°S was detected at deeper depth (~350 m) on track-1, compared to a depth of 100 m on track-2 and its thickness varied from zero to 1.2 m on track-1 and from 0.5 to 2.5 m on track-2. The thermohaline structure revealed the northward subduction of a mixture of AASW and SASW up to 45.5°S and down to 500 (320) m on track-1 (track-2).

The Antarctic domain, which extended to the shelf from 53°S (58.8°) on track-1 (track-2), was dominated by the AASW and SASW from the surface to ~100 m (180). On track-1 (track-2), the WW was marked by a minimum temperature of −1.1°C (−1.4°) and occupied upper 100 m (122) from SB to 66°S (AD). A novel finding was the detection of a layer of freshwater in the upper 30 m capped the high salinity water below 50 m, which descended the continental slope and occupied the entire water column to the south of AD. The volume transport across track-1 (track-2) amounted to 4.4 Sv (5.1), while the HC/SC was found to be reduced by 35%/36% compared to that for track-1, due to the sinking of the cold and low saline AASW and SASW.

Author's contribution

Luis formulated the project, sought funds, and offered technical advice on data collection to expedition member Mr. Kiledar, prepared figures, and edited/revised the manuscript, while Mr. Ashutosh assisted in data quality control.

Declaration of competing interest

The authors declare that they have no known competing financial interests or personal relationships that could have appeared to influence the work reported in this paper.

Acknowledgments

We acknowledge the Ministry of Earth Sciences, Govt. of India, New Delhi, India for funding the XCTD probes. NCPOR Director, Dr. M. Ravichandran is acknowledged for infrastructural facilities, and Mr. Javed Beg, Group Director, for Antarctic logistic support. MADT was downloaded from https://las.aviso.oceanobs.com/las/, and merged microwave *Ts* data are produced by Remote Sensing Systems and sponsored by NASA Physical Oceanography Program. GrADS was used to make 2-D plots. Two anonymous reviewers offered constructive comments which improved the first draft version. We also thank Prof. Igor Belkin, editor-in-chief for his suggestions for improvement of the manuscript.

References

Anilkumar, N., Luis, A.J., Somayajulu, Y.K., Babu, V.R., Dash, M.K., Pednekar, S.M., Babu, K.N., Sudhakar, M., Pandey, P.C., 2006. Fronts, water masses, and heat content variability in the western Indian sector of the Southern Ocean during austral summer 2004. J. Mar. Syst. 63, 20–34.

Anilkumar, N., George, J.V., Chacko, R., Nuncio, M., Sabu, P., 2015. Variability of fronts, fresh water input and chlorophyll in the Indian Ocean sector of the Southern Ocean. N. Z. J. Mar. Freshw. Res. 49 (1) https://doi.org/10.1080/00288330.2014.924972.

Belkin, I.M., Gordon, A.L., 1996. Southern Ocean fronts from the Greenwich meridian to tasmania. J. Geophys. Res. 101, 3675–3696.

Botnikov, V.N., 1963. Geographical position of the antarctic convergence zone in the pacific ocean. Sov. Antarct. Exped.Inf.Bull.Engl. Transl 4, 324–327.

Chambers, D.P., 2018. Using kinetic energy measurements from altimetry to detect shifts in the positions of fronts in the Southern Ocean. Ocean Sci. 14, 105–116.

CMEMS (Producer), 2017. CMEMS ONLINE CATALOGUE. COPERNICUS Marine Environment Monitoring Service. Retrieved from. http://marine.copernicus.eu/services-portfolio/access-to-products/?option=com_csw&view=details&product_id=SEALEVEL_GLO_PHY_L4_NRT_OBSERVATIONS_008_046.

CSIRO Cookbook, 1993. CSIRO Cookbook for Quality Control of Expendable Bathythermograph (XBT) Data. CSIRO, Hobart, Tasmania, p. 74.

Cunningham, S.A., Alderson, S.G., King, B.A., et al., 2003. Transport and variability of the antarctic circumpolar current in Drake passage. J. Geophys. Res. 108 (C5), 8084. https://doi.org/10.1029/2001001147.

Deacon, G.E.R., 1937. The hydrology of the Southern Ocean. Discov. Rep. 15, 3–122.

Dong, S., Sprintall, J., Gille, S.T., Talley, L., 2008. Southern Ocean mixed-layer depth from Argo float profiles. J. Geophys. Res. 113, C06013. https://doi.org/10.1029/2006JC004051.

Dong, S., Sprintall, J., Gille, S.T., 2006. Location of the Antarctic Polar Front from AMSR-E satellite sea surface temperature measurements. J. Phys. Oceanogr. 36, 2075–2089. https://doi.org/10.1175/JPO2973.1.

Donohue, K.A., Toole, J.M., 2003. A near-synoptic survey of the southwest Indian Ocean. Deep-Sea Res., Part II 50, 1893–1931. https://doi.org/10.1016/S0967-0645(03)00039-0.

Fahrbach, E., Rohardt, G., Krause, G., 1992. The antarctic coastal current in the southeastern Weddell Sea. Polar Biol. 12 (2), 171–182. https://doi.org/10.1007/BF00238257.

Freeman, N.M., Lovenduski, N.S., 2016. Mapping the antarctic polar front: weekly realizations from 2002 to 2014. Earth Syst. Sci. Data 8, 191–198. https://doi.org/10.5194/essd-8-191-2016.

Ganachaud, A., Wunsch, C., 2000. Improved estimates of global ocean circulation, heat transport and mixing from hydrographic data. Nature 408, 453–457.

Georgi, S.T., Toole, J.M., 1982. The Antarctic Circumpolar Current and the oceanic heat and freshwater budgets. J. Mar. Res. 40, 183–197.

Gille, S.T., 2002. Warming of the Southern Ocean since the 1950s. Science 295 (5558), 1275–1277.

Gordon, A.L., 1981. South Atlantic thermohaline ventilation. Deep-Sea Res. 28, 1239–1264.

Gordon, A.L., 1985. Indian-Atlantic transfer of thermohaline water of the Agulhas retroflection. Science 227, 1030–1033.

Gordon, A.L., Lutjeharms, J.R.E., Gründlingh, M.L., 1987. Stratification and circulation at the Agulhas retroflection. Deep-sea res. Part 1. Oceanogr. Res. Pap. 34 (4), 565–599.

Graham, R.M., de Boer, A.M., Heywood, K.J., Chapman, M.R., Stevens, D.P., 2012. Southern Ocean fronts: controlled by wind or topography? J. Geophys. Res. 117, C08018. https://doi.org/10.1029/2012JC007887.

Holliday, N.P., Read, J.F., 1998. Surface oceanic fronts between Africa and Antarctica. Deep-Sea Res. Part I 45, 217–238.

Kim, Y.S., Orsi, A.H., 2014. On the variability of Antarctic Circumpolar Current fronts inferred from 1992-2011 altimetry. J. Phys. Oceanogr. 44, 3054–3071.

Kizu, S., Onishi, H., Suga, T., Hanawa, K., Watanabe, T., Iwamiya, H., 2008. Evaluation of the fall rates of the present and developmental XCTDs. Deep-Sea Res. Part 1 (55), 571–586.

Klyausov, V.D., 1983. On the frontal zone near the northern boundary of sea ice distribution in the Southern Ocean. Engl. Trans.) Oceanology 33 (6), 727–734.

Koblinsky, C.J., 1990. The global distribution of f/H and the barotropic response of the ocean. J. Geophys. Res. 95 (C3), 3213–3218.

Kostianoy, A.G., Ginzburg, A.I., Frankignoulle, M., Delille, B., 2004. Fronts in the Southern Indian Ocean as inferred from satellite sea surface temperature data. J. Mar. Syst. 45, 55–73.

Laxenaire, R., Speich, S., Blanke, B., Chaigneau, A., Pegliasco, C., Stegner, A., 2018. Anticyclonic eddies connecting the western boundaries of Indian and Atlantic Oceans. J. Geophys. Res. 123, 7651–7677.

Lovenduski, N.S., Gruber, N., 2005. Impact of the southern annular mode on Southern Ocean circulation and biology. Geophys. Res. Lett. 32, L11603. https://doi.org/10.1029/2005GL022727.

Luis, A.J., Sudhakar, M., 2009. Upper-ocean hydrodynamics along meridional sections in the southwest Indian sector of the Southern Ocean during austral summer 2007. Pol. Sci. 3 (1), 13–30.

Luis, A.J., Pednekar, S.M., 2010. Hydrodynamics between Africa and Antarctica during austral summer 2008. J. Mar. Syst. 83, 45–57.

Lutjeharms, J.R.E., Valentine, H.R., Van Ballegooyen, R.C., 1993. On the subtropical convergence in the south Atlantic Ocean. South Afr. J. Sci. 89, 552–559.

Lutjeharms, J.R.E., Valentine, H.R., 1984. Southern Ocean thermal fronts south of Africa. Deep-Sea Res. Part I 31, 1461–1475.

Lutjeharms, J.R.E., Ansorge, I.J., 2001. The Agulhas Return current. J. Mar. Syst. 30 (1–2), 115–138.

Lutjeharms, J.R.E., 1972. A quantitative assessment of year-to-year variability in water movement in the southwest Indian Ocean. Nature 239, 59–60.

Macdonald, A., Wunsch, C., 1996. An estimate of global ocean circulation and heat fluxes. Nature 382, 436–439.

Meijers, A.J.S., Klocker, A., Bindoff, N.L., Williams, G.D., Marsland, S.J., 2010. The circulation and water masses of the Antarctic shelf and continental slope between 30 and 80° E. Deep-Sea Res. Part II. Topical Studies in Oceanogr 57, 723–737.

Mazloff, M., Heimbach, P., Wunsch, C., 2010. An eddy-permitting Southern Ocean state estimate. J. Phys. Oceanogr. 40 (5), 880–899.

Millero, F.J., Poisson, A., 1981. International one-atmosphere equation of state of seawater. Deep Sea Res., Part A, Oceanogr. Res. Papers 28, 625–629.

Mizuno, K., Watanabe, T., 1998. Preliminary results of the insitu XCTD/CTD comparison test. J. Oceanogr. 54, 373–380.

Middleton, J.H., Humphries, S.E., 1989. Thermocline structure and mixing in the region of Prydz Bay, Antarctica. Deep-Sea Res. Part 1. Oceanogr. Res. Pap. 36, 1255–1266.
Orren, M.J., 1966. Hydrology of the South West Indian Ocean. Investigational Report of the Division for Sea Fisheries of S. Africa, vol. 55, pp. 1–35.
Orsi, A.H., Whitworth III, T., Nowlin Jr., W.D., 1995. On the meridional extent and fronts of the Antarctic Circumpolar Current. Deep Sea Res. Oceanogr. Res. Pap. 42, 641–673.
Park, Y.-H., Gamberoni, L., Charriaud, E., 1993. Frontal structure, water masses and circulation in the Crozet Basin. J. Geophys. Res. 98, 12361–12385.
Park, Y.-H., Charriaud, E., Fieux, M., 1998. Thermocline structure of the Antarctic surface water/winter water in the Indian sector of the Southern Ocean. J. Mar. Syst. 17, 5–23.
Park, Y.-H., Charriaud, E., Craneguy, P., 2001. Fronts, transport, and Weddell gyre at 30°E between Africa and Antarctica. J. Geophys. Res. 106, 2857–2879.
Peterson, R.G., Whitworth, T., 1989. The subantarctic and polar fronts in relation to deep water masses through the southwestern Atlantic. J. Geophys. Res. 94 (C8), 10817–10838.
Pollard, R., Lucas, M., Read, J., 2002. Physical controls on biogeochemical zonation in the Southern Ocean. Deep Sea Res., Part II 49, 3289–3305.
Renault, A., Provost, C., Sennéchael, N., Barré, N., Kartavtseff, A., 2011. Two full-depth velocity sections in the Drake Passage in 2006—Transport estimates. Deep-Sea Res. Part II 58, 2572–2591.
Rintoul, S.R., Sokolov, S., 2001. Baroclinic transport variability of the Antarctic Circumpolar Current south of Australia (WOCE repeat section SR3). J. Geophys. Res. 106, 2815–2832.
Sloyan, B.M., Rintoul, S.R., 2001. Circulation, renewal and modification of Antarctic mode and intermediate water. J. Phys. Oceanogr. 32, 1005–1030.
Smith, W.H.F., Sandwell, D.T., 1997. Global sea floor topography from satellite altimetry and ship depth soundings. Science 277 (5334), 1956–1962.
Smith, N.R., Zhaoqian, D.J., Kerry, K.R., Wright, S., 1984. Water masses and circulation in the region of Prydz Bay, Antarctica. Deep-Sea Res. Part I 31, 1121–1147.
Sokolov, S., Rintoul, S.R., 2002. Structure of Southern Ocean fronts at 140°E. J. Mar. Syst. 37 (1-3), 151–184.
Sokolov, S., Rintoul, S.R., 2007. Multiple jets of the antarctic circumpolar current south of Australia. J. Phys. Oceanogr. 37, 1394–1412.
Sparrow, M.D., Heywood, K.J., Brown, J., Stevens, D.P., 1996. Current structure of the south Indian Ocean. J. Geophys. Res. 101, 6377–6391.
Speich, S., Blanke, B., Madec, G., 2001. Warm and cold water routes of an OGCM thermohaline conveyor belt. Geophys. Res. Lett. 28, 311–314.
Stramma, L., 1992. the South Indian Ocean Current. J. Phys. Oceanogr. 22, 421–430.
Stramma, L., Lutjeharms, J.R.E., 1997. The flow field of the subtropical gyre of the south Indian Ocean. J. Geophys. Res. 102 (C3), 5513–5553.
Swart, N.C., Gille, S.T., Fyfe, J.C., Gillett, N.P., 2018. Recent Southern Ocean warming and freshening driven by greenhouse gas emissions and ozone depletion. Nat. Geosci. 11, 836–841.
Swart, S., Speich, S., Ansorge, I.J., Goni, G.J., Gladyshev, S., Lutjeharms, J.R.E., 2008. Transport and variability of the antarctic circumpolar current south of Africa. J. Geophys. Res. 113, C09014. https://doi.org/10.1029/2007JC004223.
Swart, S., Speich, S., 2010. An altimetry-based gravest empirical mode south of Africa: 2. Dynamic nature of the Antarctic Circumpolar Current fronts. J. Geophys. Res. 115, C03003.
Tsubouchi, T., Suga, T., Hanawa, K., 2010. Indian Ocean Subtropical Mode Water: its water characteristics and spatial distribution. Ocean Sci. 6, 41–50.
Uchida, H., Shimada, K., Kawano, T., 2011. A method for data processing to obtain high-quality XCTD data. J. Atmos. Ocean. Technol. 28, 816–826.
Vernet, M., Geibert, W., Hoppema, M., Brown, P.J., Haas, C., Hellmer, H.H., et al., 2019. The Weddell gyre, Southern Ocean: present knowledge and future challenges. Rev. Geophys. 57, 623–708. https://doi.org/10.1029/2018RG000604.
Valentine, H.R., Lutjeharms, J.R.E., Brundrit, G.B., 1993. The water masses and volumetry of the southern Agulhas Current region. Deep Sea Res. 40 (6), 1285–1305 part 1.
Whitworth, T., 1985. The net transport of the antarctic circumpolar current through Drake passage. J. Phys. Oceanogr. 12 (9), 960–971.
Whitworth III, T., Nowlin Jr., W.D., 1987. Water masses and currents of the southern ocean at the Greenwich Meridian. J. Geophys. Res. 92, 6462–6476, 1987.
Wong, A.P.S., Bindoff, N.L., Forbes, A., 1998. Oceane ice shelf interaction and possible bottom water formation in Prydz Bay, Antarctica. In: Jacobs, S.S., Weiss, R.F. (Eds.), Ocean, Ice and Atmosphere: Interactions at the Antarctic Continental Margin. Antarctic Research Ser., vol. 75. AGU, Washington D.C., pp. 173–187
Yuan, X., Martinson, D.G., Dong, Z., 2004. Upper-ocean thermohaline structure and its temporal variability in the southeast Indian Ocean. Deep Sea Res. Oceanogr. Res. Pap. 51, 333–347.